Journal Homepage: http://ijcpe.uobaghdad.edu.iq
Iraqi Journal of Chemical and Petroleum Engineering
Vol. 26 No. 4 (December 2025) 73 – 88
EISSN: 2618-0707, PISSN: 1997-4884

Effect of Fe(II) addition by ion exchange and precipitation of different semiconductors on the textural properties of 13X zeolite

Rawan H. Ali [a], Sami M. Zaboon [a], and Ammar S. Abbas [a, *]

a Chemical Engineering Department, College of Engineering, University of Baghdad, Baghdad, Iraq

Abstract

This study investigated the textural properties of 13X zeolite, FeX zeolite, TiO_2/FeX zeolite, ZnO/FeX zeolite, and TiO_2+ZnO/FeX zeolite using nitrogen adsorption-desorption data at consistent low temperatures. The adsorption-desorption isotherm indicated that the studied materials have a type IV mesoporous structure, as defined by the International Union of Pure and Applied Chemistry. The results of nitrogen adsorption data analysis using the Langmuir, Freundlich, and Brunauer-Emmett-Teller models indicated that the data were best described by the Brunauer-Emmett-Teller model. The Barrett, Joyner, and Halenda model was used to analyze the pore size distribution, pore diameter, and average pore volume of the adsorbents. After the ion exchange and loading process, there was a notable decrease in surface area and pore size distribution values, while the reduction in pore volume was minimal. Zeolite 13X showed a larger pore diameter, suggesting that some structural damage or the formation of wider pores within the mesoporous range occurred during the ion exchange steps or modification by the addition of semiconductor oxides. In contrast, the FeX zeolite exhibited a smaller pore size, indicative of a more compact microporous structure. While the modified zeolites—TiO_2, ZnO, and TiO_2+ZnO—demonstrated a consistent pore structure, suggesting stable mesoporosity with a smaller pore size, this implies that some of the zeolite's pores were blocked or filled with TiO_2 and ZnO particles.

Keywords: Adsorption-Desorption; physisorption isotherms; mesoporous structure; pore size distribution; surface area.

Received on 02/06/2025, Received in Revised Form on 14/10/2025, Accepted on 14/10/2025, Published on 30/12/2025

https://doi.org/10.31699/IJCPE.2025.4.7

1- Introduction

Zeolites are crystalline, porous substances primarily composed of aluminum, silicon, and oxygen, which form the essential structural components [1]. Nanomaterials feature at least one nanoscale structural element (ranging from 1 to 100 nm), which gives rise to various distinct properties and facilitates a wide array of applications. According to the International Union of Pure and Applied Chemistry, porous materials are classified into three primary categories: microporous materials with pore sizes under 2 nm, mesoporous materials with pore sizes between 2 and 50 nm, and macroporous materials with pore sizes exceeding 50 nm [2]. As crystalline silicates, zeolites possess three-dimensional frameworks composed of tetrahedra that create uniform pores [3]. Each pore is bordered by four oxygen atoms surrounding a central cation, providing a unique viewpoint for adsorption and catalysis, particularly when subjected to heat [4].

The zeolite framework is composed of aluminum and silicon coordinated tetrahedrally with oxygen, along with water molecules. Also, the chemical composition of zeolites usually contains mono- or divalent metal ions such as sodium, potassium, magnesium, calcium, and barium [5]. The physical and chemical properties of zeolites change based on the Si/Al ratio. A low Si/Al ratio (1 to 2) creates a hydrophilic surface, while a high ratio (10 and above) leads to a hydrophobic surface [6]. Low-silica zeolites, which are highly hydrophilic, exhibit stronger interactions with polar molecules, such as water [7]. The Si/Al ratio typically reflects the structural type that offers chemical and thermal stability, influencing zeolite applications. In X-type zeolite, the Si/Al ratio is between 2 and 5, while in Y-type zeolite, it is 3 or higher [8]. Expanding zeolite usage involves structural modifications; ion exchange reactions using cationic surfactants significantly alter the surface properties of zeolites. Zeolite is crucial to adjust the chemical makeup and content of ion exchange materials through appropriate pretreatment. In order to enhance ion exchange efficiency and create a porous material with high adsorption capacity, the zeolite should possess a large specific surface area and a porous structure rich in micropores. Moreover, due to its distinctive pore size, zeolite can hold water and exchangeable cations within its crystalline and porous framework [9-11].

Zeolites are extensively used for various purposes, such as adsorbents [12, 13], sorbents for dyes [14, 15], heavy metals [16, 17], and various contaminants in both wastewater and natural water [18]. Additionally, zeolites are used as molecular filters [19], ion exchange materials [20], and catalysts [21]. Zeolites are generally divided into two main types: natural and synthetic, each possessing unique properties and applications [22-25].

*Corresponding Author: Email: ammarabbas@coeng.uobaghdad.edu.iq

Natural zeolites typically form through the interaction between groundwater and sedimentary rocks. Common variations include Clinoptilolite, Mordenite, Chabazite, Phillipsite, and Analcime. The industrial applications of natural zeolites are limited, as their properties are closely tied to their crystal structures, and the channel diameters, ranging from 0.30 to 4 nm, prevent the adsorption of larger gas molecules and organic compounds [26, 27].

Synthetic zeolites are created by heating materials such as China clay, feldspar, and soda ash [23, 28]. Research has identified over 200 varieties of synthetic zeolites [29], including zeolite A, X, Y, ZSM5, and Beta [4]. Although zeolites offer numerous benefits and play a significant role in chemical processes, they also have drawbacks. The main challenge is that when the sizes of reactants are comparable to or exceed micropores, access to active sites becomes restricted, leading to diffusion difficulties. In the production of nano zeolites, a notable increase in external surface area is achieved, producing hierarchical zeolites that enhance diffusion pathways [30].

Numerous techniques have been developed to synthesize hierarchical zeolites, which can be broadly categorized into two primary groups: top-down and bottom-up methods [30]. Moreover, zeolites exhibit several characteristics, including molecular sieving, shape selectivity, large surface area, adjustable pore sizes, exceptional thermal and hydrothermal stability, customizable acidity, crystallinity, and ion exchange capabilities [31-33].

Zeolite X has a Faujasite-type structure, making it a valuable model for natural zeolites [27, 34], and its framework exhibits a tetrahedral arrangement of sodalite elements or truncated octahedra. Each sodalite component contains six square oxygen atom faces and eight hexagonal faces, creating an enhanced structure that defines zeolite X [35]. Zeolite X structure features substantial cavities, either spherical or elliptical, approximately 13 Å in diameter, referred to as supercages, which are accessed through channels measuring 8-9 Å in diameter. At the same time, the interior of the truncated octahedron incorporates smaller cavities roughly 6.6 Å in diameter, with an entrance through the hexagonal face of about 2.2 Å. In zeolite type 13X, the negative charge is offset by an adequate number of cations, facilitating electrostatic interactions [36]. Zeolite 13X has a low Si/Al ratio in its framework, which translates into high ion exchange capacity, strong sorption abilities, and a relatively large pore size that maximizes photoactivity, positioning it as an optimal adsorbent among various zeolites [36].

Heterogeneous photocatalysis has emerged as a highly effective strategy for the degradation and total mineralization of persistent organic pollutants [37], attracting significant scientific and industrial interest [38, 39]. Various catalysts have been investigated to degrade phenol through light irradiation. Among these, titanium dioxide (TiO_2) and zinc oxide (ZnO), which are semiconducting photocatalysts, hold a prominent position in photocatalysis [40]. TiO_2 has a bandgap energy (Eg) between 3.0 and 3.2 eV, requiring excitation by light wavelengths shorter than approximately 400 nm [41], enabling it to decompose toxic organic pollutants in water by generating hydroxyl radical with high oxidation potential. TiO_2 exists in three crystalline forms: anatase and rutile, which are the most common, and brookite, an orthorhombic structure that is rarely utilized [42]. Rutile's crystalline size is always greater than that of the anatase phase. ZnO is also a prevalent and low-cost material, making it one of the most promising substances for the development of new environmental technologies [43, 44]. The properties of the ZnO semiconductor make this oxide a catalyst for the degradation of several recalcitrant substances through heterogeneous photocatalysis [45]. The band gap of bulk ZnO is 3.44 eV at low temperatures and 3.37 eV at room temperature [46], a value nearly identical to that of TiO_2.

This study examines the textural characteristics of 13X zeolite and its modified forms, including Fe (II)-exchanged FeX zeolite, and synthesizing TiO_2/FeX zeolite, ZnO/FeX zeolite, and TiO_2+ZnO/FeX zeolite via the impregnation technique, using the N_2 adsorption-desorption method. The data gathered will be fitted to multiple adsorption isotherms, including the Langmuir, Freundlich, and Brunauer-Emmett-Teller (BET) methods, to calculate the BET surface area (S_{BET}) and assess the total surface area. At the same time, the Halsey equation will be used to calculate the thickness of the adsorbed layer on the pore walls. Additionally, the Barrett-Joyner-Halenda (BJH) method will provide information on pore size distribution, pore diameter (d_{BJH}), and pore volume (V_p).

2- Experimental work

2.1. Chemicals

All chemicals used in the research were obtained from local markets and supplied by various companies. Unmodified zeolite 13X ($Na_{86}[(AlO_2)_{86}(SiO)_{106}].H_2O$) provided by Sigma-Aldrich (Germany). The ion exchange process required the use of 35-38% hydrochloric acid (HCl) and hydrated ferrous sulfate ($FeSO_4 \cdot 7H_2O$), both of which were supplied by SDFCL and COH (India). Absolute ethanol (C_2H_5OH) with 99.5% purity (Scharlab, Spain) was used in the surface modification process with the semiconductors, which were titanium dioxide (TiO_2 nanoparticles) with 99.5% purity from US Research Nanomaterials, Inc., and zinc oxide (ZnO nanoparticles) with 99.8% purity from Skyspring Nanomaterials, Inc. (USA).

2.2. Modification of 13X zeolite catalyst

Zeolite 13X was ground into a fine powder and sieved to yield particles with a size range of 70 to 99 micrometers (μm). The sieved zeolite underwent thorough washing with distilled water and deionized water to eliminate impurities. The washed 13X zeolite was filtered through filter paper using a Buchner funnel and a vacuum pump, then dried overnight in an oven. Subsequently, the

dried 13X zeolite was treated with a 0.1 M HCl solution at a ratio of 10:1 (HCl solution volume to zeolite weight) and then separated using filter paper. The treated 13X zeolite was washed repeatedly with distilled water until its pH reached 7, dried overnight at 60 °C, and calcinated at 550 °C for 3 hours. The calcined 13X zeolite was then submitted to an ion exchange process, which was carried out at 80 °C for 8 hours and involved a 0.319 M solution of ferrous sulfate heptahydrate ($FeSO_4 \cdot 7H_2O$) as a source of iron to replace the sodium ions in the zeolite. The exchanged 13X zeolite was washed and filtered multiple times with deionized water to remove any unexchanged Fe (II). The modified catalyst was subsequently dried overnight in an oven and finally calcined at 550 °C for 3 hours.

2.3. Addition of the semiconductors (TiO_2 and ZnO)

Two types of semiconductors, TiO_2 and ZnO, were employed to produce three catalyst variants: TiO_2/FeX zeolite, ZnO/FeX zeolite, and TiO_2+ZnO/FeX zeolite through the solid-state dispersion technique. Five grams of FeX zeolite were suspended in 55 mL of absolute ethanol at room temperature. Then, a semiconductor comprising 10% by weight of the catalyst and the mixture was stirred for 10 hours. The catalyst was then dried by evaporation at 110°C and finally calcined at 450°C for 5 hours.

2.4. Adsorption-desorption measurements

N_2 adsorption and desorption amounts (in cm^3/g) were measured for samples of 0.3246 g for 13X zeolite, 0.1519 g for FeX zeolite, 0.1781 g for TiO_2/FeX zeolite, 0.1268 g for ZnO/FeX zeolite, and 0.1913 g for TiO_2+ZnO/FeX zeolite, using BELsorp, Mini2, JAPAN instrument. Subsequently, data were taken to study adsorption-desorption isotherms, determine the specific surface area (S_{BET}), particle size distribution, pore diameter, and pore volume (V_p).

3- Theoretical work

3.1. Langmuir isotherm model

The Langmuir isotherm is an empirical model that assumes adsorption occurs at a limited number of well-defined, localized sites, forming a single molecular layer (monolayer adsorption) on the surface [47]. Eq. 1 can represent the linear form of the Langmuir isotherm model.

$$\frac{P}{V} = \frac{P}{V_m} + \frac{1}{V_m K_L} \quad (1)$$

In this context, P (mmHg) denotes the equilibrium pressure, and V (cm^3/g (STP)) refers to the volume of nitrogen adsorbed at a specific pressure and constant temperature. Meanwhile, V_m (cm^3/g (STP)) indicates the maximum volume of nitrogen that can be adsorbed to create a complete monolayer on the solid surface. The term K_L (1/mmHg) represents a Langmuir constant, reflecting the degree of interaction between the gas and the solid surface, which correlates with variations in surface area and porosity of the adsorbent. This model suggests that a larger surface area and pore volume (V_P) result in increased adsorption capacity [48]. Plotting P/V against P should produce a straight line, where the slope and intercept are utilized to calculate the monolayer maximum adsorption capacity and the Langmuir constant.

3.2. Freundlich isotherm model

The Freundlich isotherm represents a mathematical relationship that characterizes non-ideal and reversible adsorption processes, making it one of the earliest established models in this field. Freundlich isotherm applies to multilayer adsorption, assuming energetic heterogeneity throughout the adsorbent surface. The model's linear expression can be depicted as Eq. 2 [49].

$$\ln V = \ln K_f + \frac{1}{n} \ln P \quad (2)$$

Here, V (cm^3/g (STP)) refers to the volume of nitrogen adsorbed at a specific pressure and constant temperature. In contrast, the Freundlich constant is denoted by K_f, and n represents the heterogeneity factor [49].

3.3. BET isotherm model

The BET isotherm is regarded as one of the most reliable methods for determining the surface area of solid materials. The surface area is assessed using the BET equation, which is based on a specific section of the gas adsorption isotherm. The analysis isotherm relies on adsorption isotherms of inert gas molecules, such as nitrogen or argon, over a pressure range that includes monolayer coverage. The BET isotherm serves as a theoretical equation for calculating the surface area of gas-solid equilibrium systems Eq. 3 [50].

$$\frac{\left(\frac{P}{P^\circ}\right)}{V\left[1-\left(\frac{P}{P^\circ}\right)\right]} = \frac{C-1}{V_m C}\left(\frac{P}{P^\circ}\right) + \frac{1}{V_m C} \quad (3)$$

Where: V (cm^3/g (STP)) represents the volume of nitrogen adsorbed at a specified pressure and constant temperature, V_m (cm^3/g (STP)) denotes the maximum volume of nitrogen that can be adsorbed to achieve a complete monolayer on the solid surface. At the same time, C consistently reflects the difference between the heat of adsorption in the first layer and the heat of vapor-liquefaction.

Applying the BET equation to the nitrogen adsorption data obtained was only possible within a narrow range of relative pressures (ranging from 0.05 to 0.3) [51]. A plot of $\left(\frac{P}{P^\circ}\right) \Big/ \left(V\left(1-\left(\frac{P}{P^\circ}\right)\right)\right)$ versus $\left(\frac{P}{P^\circ}\right)$ should yield a straight line with a positive slope, then V_m and C can be determined from the intercept and slope [52].

3.4. Evaluation of the total surface area

The assessment of the aggregate surface area of the samples was implemented utilizing Eq. 4.

$$SA = \frac{V_m N A_m}{V} \quad (4)$$

Where: N is Avogadro number (6.0221 x 10^{23} mol^{-1}), A_m is the cross-sectional area of the adsorbate and equals 0.162 nm^2, and V is the molar volume for nitrogen, which equals 22414 cm^3/mol.

3.5. Thickness of the adsorbed layer

The Halsey equation (Eq. 5) offers a method to calculate the thickness of the adsorbed layer left on the pore walls [53].

$$t = 3.54\left(\frac{-5}{\ln\left(\frac{P}{P^\circ}\right)}\right)^{0.333} \quad (5)$$

3.6. BJH pore diameter and volume

The BJH method determines desorption pore diameter (d_{BJH}) and the pore volume (V_p) of the adsorbent from experimental data by examining N_2 adsorption-desorption isotherm data. The BJH model was developed in 1951 [54], based on the assumption that all pores are cylindrical, nonintersecting, and have open ends. The pore radius is regarded as the sum of the Kelvin radius and the thickness of the adsorbed layer, as noted in the adsorption process Eq. 6 [55, 56].

$$\ln\left(\frac{P}{P^\circ}\right) = -\frac{2\gamma v \cos\theta}{RT(r-t)} \quad (6)$$

Where: (r - t) represents the average pore radius, γ denotes the surface tension of the adsorbate in N/m, ν indicates the molar volume of the adsorbate, θ is the contact angle between the adsorbate and adsorbent (assumed to be 0°) in m^3/mole, R is the gas constant, valued at 8.314 J/K mole, and T refers to the absolute temperature in K.

4- Results and discussion

4.1. N_2 physisorption isotherms

The N_2 isotherms for 13X zeolite, FeX zeolite, TiO_2/FeX zeolite, ZnO/FeX zeolite, and TiO_2+ZnO/FeX zeolite were shown in Fig. 1. The adsorption isotherm, represented by the thick line, plots P/P° from zero to vacuum of the absorbate against the amount of N_2 adsorbed, known as adsorption. Conversely, adjusting the isotherm to vacuum pressure yields a well-defined dashed line, termed desorption, as displayed in Fig. 1.

The maximum amounts of N_2 adsorbed at P/P° for the samples were 52.13 cm^3/g for 13X zeolite. After the ion exchange process, the adsorption amount increased to 173.79 cm^3/g for FeX zeolite. The increase in Fe content in FeX zeolite after ion exchange is attributed to the successful substitution of Na^+ in the zeolite framework with Fe^{3+} ions from the solution, demonstrating that the zeolite possesses a high ion exchange capacity and a strong affinity for Fe^{3+} ions. The addition of TiO_2 resulted in a reduction in the adsorption rate, measuring 159.07 cm^3/g for TiO_2/FeX zeolite. The decrease in adsorption after introducing TiO_2 may stem from partial pore blockage and a reduction of specific surface area, as TiO_2 particles may coat the surface or accumulate in the pores, restricting the accessible area for adsorption. The adsorption rate continued to decline, reaching 155.75 cm^3/g for ZnO/FeX zeolite. The reduction in adsorption after adding ZnO might also be due to the formation of ZnO agglomerates on the zeolite surface, which could diminish surface uniformity and obstruct adsorption pathways, resulting in reduced efficiency. The combination of TiO_2 and ZnO produced the lowest adsorption value among all tested samples, at 150.50 cm^3/g for TiO_2+ZnO/FeX zeolite. The decrease in adsorption could be attributed to possible interactions between TiO_2 and ZnO, resulting in denser or less porous surface structures. Such structural alterations may decrease the number of available adsorption sites and hinder the diffusion of adsorbate molecules into the pores, as portrayed in Fig. 1.

The N_2 physisorption data were analyzed to identify the type of isotherm and characterize the adsorption process for the chosen zeolites. The quantity of N_2 adsorbed showed a gradual increase followed by a steep rise at high relative pressure (P/P°), as illustrated in Fig. 1, where the curve displayed a distinct hysteresis loop. The nitrogen adsorption-desorption isotherm measured at 77 K reveals type IV behavior, as classified by the IUPAC, indicating the presence of mesoporous structures. An H3 type hysteresis loop, depicted in Fig. 1(a), is characterized by its open and non-saturating properties at elevated P/P° (over 0.8), indicating capillary condensation in slit-like pores commonly observed in materials with layered or plate-like features. At lower relative pressures, nitrogen absorption increases steadily, followed by a more pronounced rise at intermediate to high P/P°, indicating multilayer adsorption and pore filling through capillary condensation.

The N_2 physisorption results for the synthesized FeX zeolite, created via ion exchange, exhibited a similar adsorption behavior to that of the 13X zeolite sample in terms of isotherm shape. However, the FeX zeolite demonstrated a significant increase in the amount adsorbed and a more pronounced hysteresis loop. According to the IUPAC classification, this behavior corresponds to a type IV isotherm with an H3-type hysteresis loop, indicating the presence of mesoporous structures with either irregular or plate-like morphologies. This outcome can be attributed to the ion exchange process, which likely modified the material's structural properties, increased the number of active surface sites, and facilitated the formation or opening of additional mesopores, ultimately enhancing the material's adsorption capacity, as illustrated in Fig. 1(b).

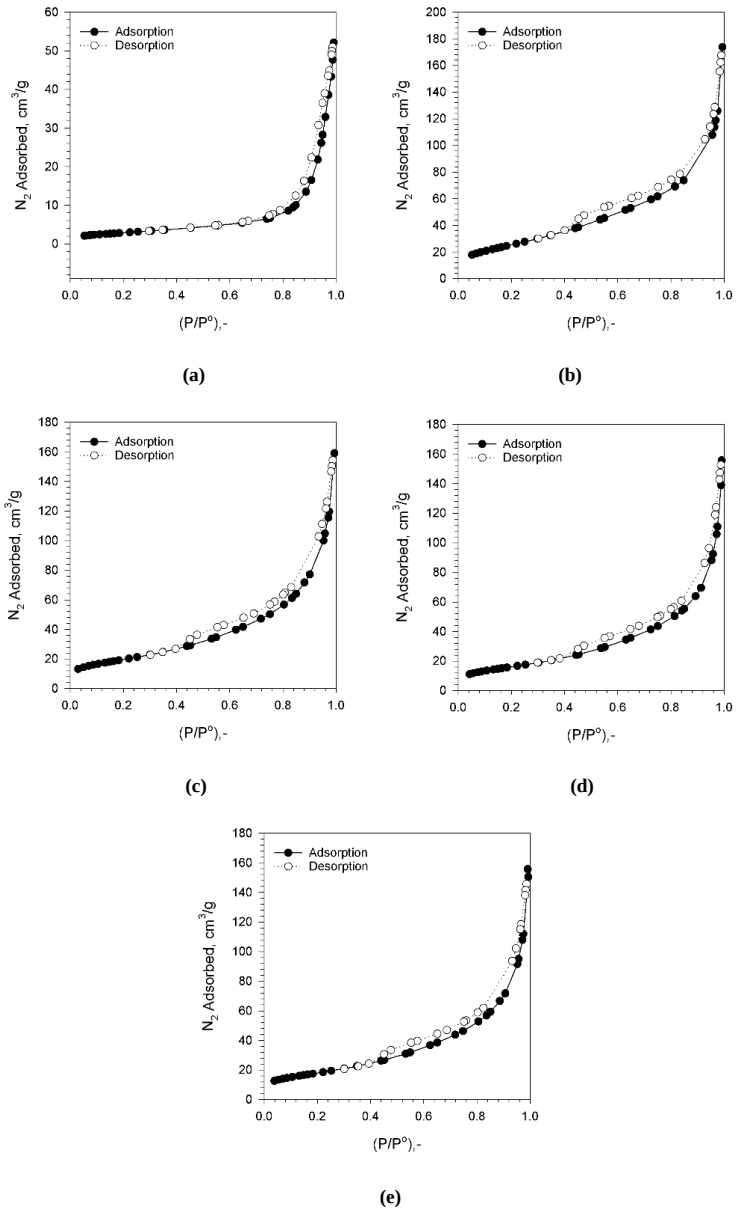

Fig. 1. N_2 adsorption-desorption isotherm for (a) 13X zeolite (b) FeX zeolite (c) TiO_2/FeX zeolite (d) ZnO/FeX zeolite (e) TiO_2+ZnO/FeX zeolite

After incorporating TiO_2 into the FeX zeolite, we observed a notable decrease in adsorption capacity, characterized by a less pronounced hysteresis loop and a slight gap between the adsorption and desorption branches, as seen in Fig. 1 (c). The alteration suggests a reduced level of mesoporosity, as indicated by a smoother isotherm and a consistent increase in adsorption. According to IUPAC classification, the TiO_2/FeX zeolite still falls under type IV and displays an H4-type hysteresis loop, which is typically associated with materials having narrow or irregular pore structures. The observed behavior is likely due to the presence of TiO_2 particles coating the surface of the FeX zeolite, which may have blocked or narrowed some mesopores, thus decreasing the number of active sites and the available surface area for adsorption compared to the 13X and FeX zeolites. After the addition of ZnO to the FeX zeolite, a further reduction in adsorption capacity was noted; however, the ZnO/FeX zeolite maintained its unique adsorption characteristics, exhibiting a clear and broader hysteresis loop, as illustrated in Fig. 1 (d). Based on the IUPAC classification, ZnO/FeX zeolite exhibits a type IV isotherm with an H2-type hysteresis loop, typically associated with irregular pores that possess narrow and complex openings. This behavior can be explained by the influence of ZnO particles on the zeolite's porous structure, which may have led to a redistribution or partial blockage of some effective pores, ultimately reducing the number of active adsorption sites. Nevertheless, some mesoporosity remained, contributing to the hysteresis pattern observed.

The TiO_2+ZnO/FeX zeolite exhibited a behavior similar to that of the ZnO/FeX zeolite regarding the shape of the adsorption curve, though with a slightly reduced hysteresis loop, as shown in Fig. 1 (e). As per IUPAC classification, the TiO_2+ZnO/FeX zeolite corresponds to a

type IV isotherm characterized by an H3 type hysteresis loop with an upward-opening shape, typically associated with slit-like or irregular pores. The slight decrease in mesoporosity is attributed to the presence of semiconductors (TiO_2 and ZnO), which may have blocked or narrowed some pores, thereby reducing the number of active adsorption sites and the overall adsorption capacity, while maintaining the material's overall mesoporous structure. The 13X zeolite displayed a narrower hysteresis loop and lower adsorption amounts compared to the other samples, as indicated in Fig. 1(a), suggesting a weaker interaction between the material surface and nitrogen molecules, along with a diminished number of effective pores. Fig. 1 (b), (c), (d), and (e) illustrate significant increases in nitrogen adsorption, indicating enhancements in surface area and pore volume after ion exchange and loading procedures. The measurements conducted at 77 K reveal a gradual adsorption trend at low P/P°, followed by a significant spike in the P/P° range from 0.45 to 0.80, reflecting multilayer adsorption and incremental pore filling. The hysteresis loops remain open, indicating slow desorption influenced by the effects of pore shape and capillary condensation.

4.2. Adsorption-desorption isotherm models

The three isotherms-Langmuir, Freundlich, and BET- and their associated mathematical models were used to characterize the N_2 adsorption behavior on the surfaces of 13X zeolite, FeX zeolite, TiO_2/FeX zeolite, ZnO/FeX zeolite, and TiO_2+ZnO/FeX zeolite.

4.2.1. Langmuir isotherm model

The Langmuir model results were obtained from experimental data using the appropriate equation (Eq. 1). Constants were calculated from the slope and intercept of the linearized version of the model, which was plotted in Fig. 2. These results indicate that the model poorly represents the adsorption process, as indicated by a low correlation coefficient (R^2) value, suggesting that adsorption does not occur on a uniform surface or as a single layer.

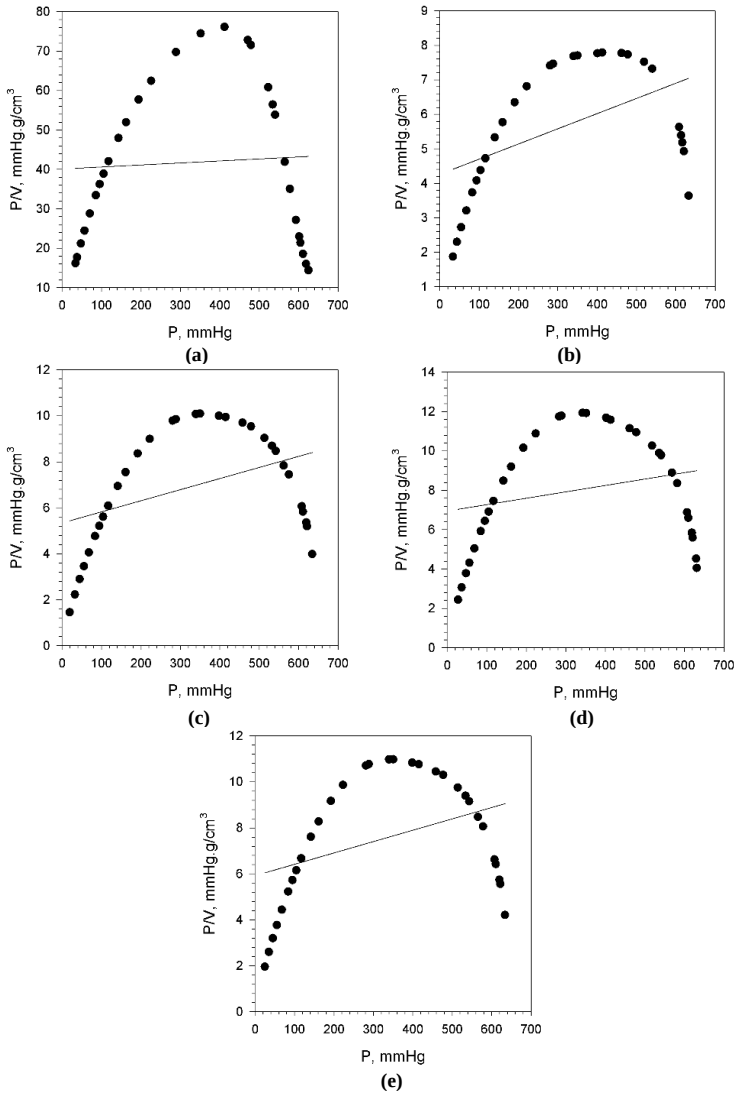

Fig. 2. N_2 adsorption isotherm by the Langmuir model for (a) 13X zeolite (b) FeX zeolite (c) TiO_2/FeX zeolite (d) ZnO/FeX zeolite (e) TiO_2+ZnO/FeX zeolite

The adsorption capacity (V_m) was measured at a low value of 74.07 cm^3/g for the 13X zeolite, demonstrating inadequate adsorption performance. After the ion exchange, the adsorption capacity significantly increased to 227.27 cm^3/g for the FeX zeolite, likely due to the creation or activation of extra adsorption sites. However, the inclusion of TiO_2 caused a decline in capacity to 208.33 cm^3/g for the TiO_2/FeX zeolite, potentially because of active site blockage or alterations in surface properties. Conversely, adding ZnO boosted the capacity to 312.50 cm^3/g for the ZnO/FeX zeolite, likely by enhancing surface reactivity. The concurrent addition of both TiO_2 and ZnO resulted in a further reduction in capacity to 204.08 cm^3/g for the TiO_2+ZnO/FeX zeolite, possibly due to interference or diminished accessibility of active sites, as in Table 1. When comparing these findings with those from a previous study [11], the adsorption capacity of NaX zeolite was found to be greater than that of the 13X zeolite, while the FeX zeolite showed a lower capacity compared to the present FeX zeolite. The variability in performance is likely due to differences in particle size, which in this study (70 to 99 µm) were larger than the 75 µm particles used previously [11]. Larger particle sizes typically result in a reduced surface-to-volume ratio, leading to a smaller available surface area and fewer active adsorption sites, which could notably affect adsorption efficiency, particularly in porous materials, where surface area and porosity play critical roles in pollutant capture.

4.2.2. Freundlich isotherm model

The physisorption of N_2 gas on the samples was assessed using Eq. 2, where plotting ln V against ln P produces a straight line with an intercept of ln K_f and a slope of 1/n, as illustrated in Fig. 3. All samples displayed straight line graphs with R^2 greater than that of Langmuir and less than that of BET, signifying a moderate interaction between the synthesized zeolites and nitrogen gas at 77 K. The "n" value indicates the adsorption intensity for the physisorption mechanism, ranging from 1.05 to 1.48 for the samples analyzed. The modified zeolites FeX and TiO_2/FeX show higher "n" values (1.5017 and 1.5436) and K_f values (1.1638 and 1.0748), respectively, in comparison to the other synthesized catalysts, as detailed in Table 1.

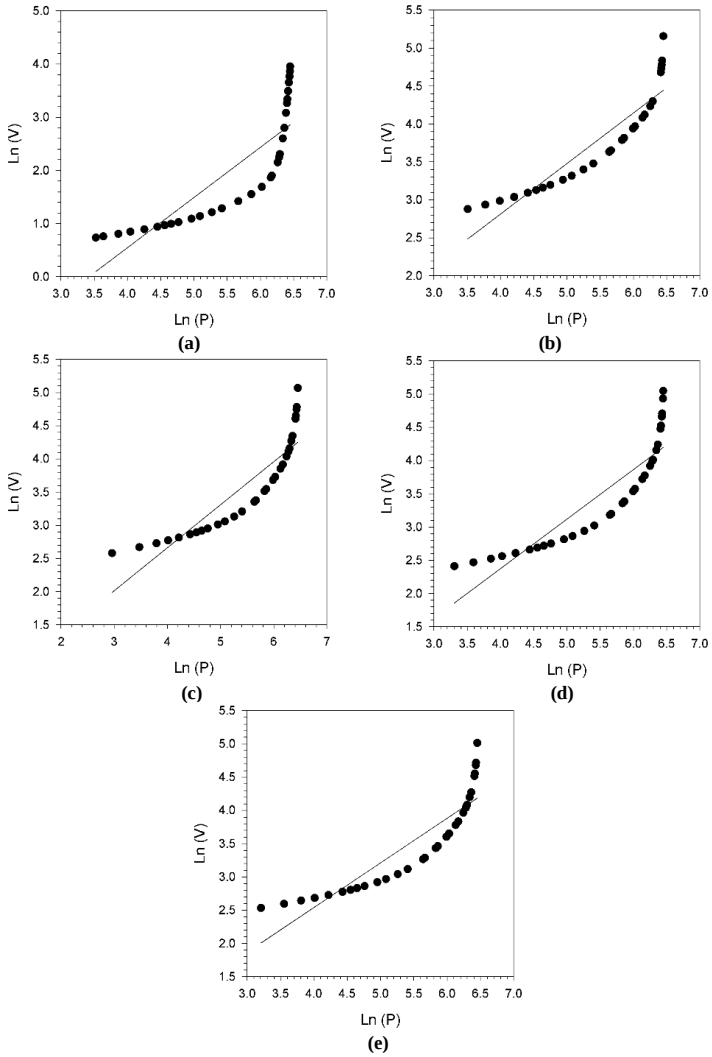

Fig. 3. N_2 adsorption isotherm by the Freundlich model for (a) 13X zeolite, (b) FeX zeolite, (c) TiO_2/FeX zeolite, (d) ZnO/FeX zeolite, (e) TiO_2+ZnO/FeX zeolite

4.2.3. BET isotherm model

The BET isotherm model (Eq. 3) aligns closely with the nitrogen adsorption data presented in Fig. 4, confirming the mesoporous nature of the samples. All five samples exhibited the highest R^2 values, as in Table 1, when fitted using the BET model, indicating that this model most accurately represents the nitrogen adsorption behavior and validates the materials' mesoporous structure. Although closely aligned with the BET model, the adsorption capacity showed erratic trends and significant variations during the different treatment phases.

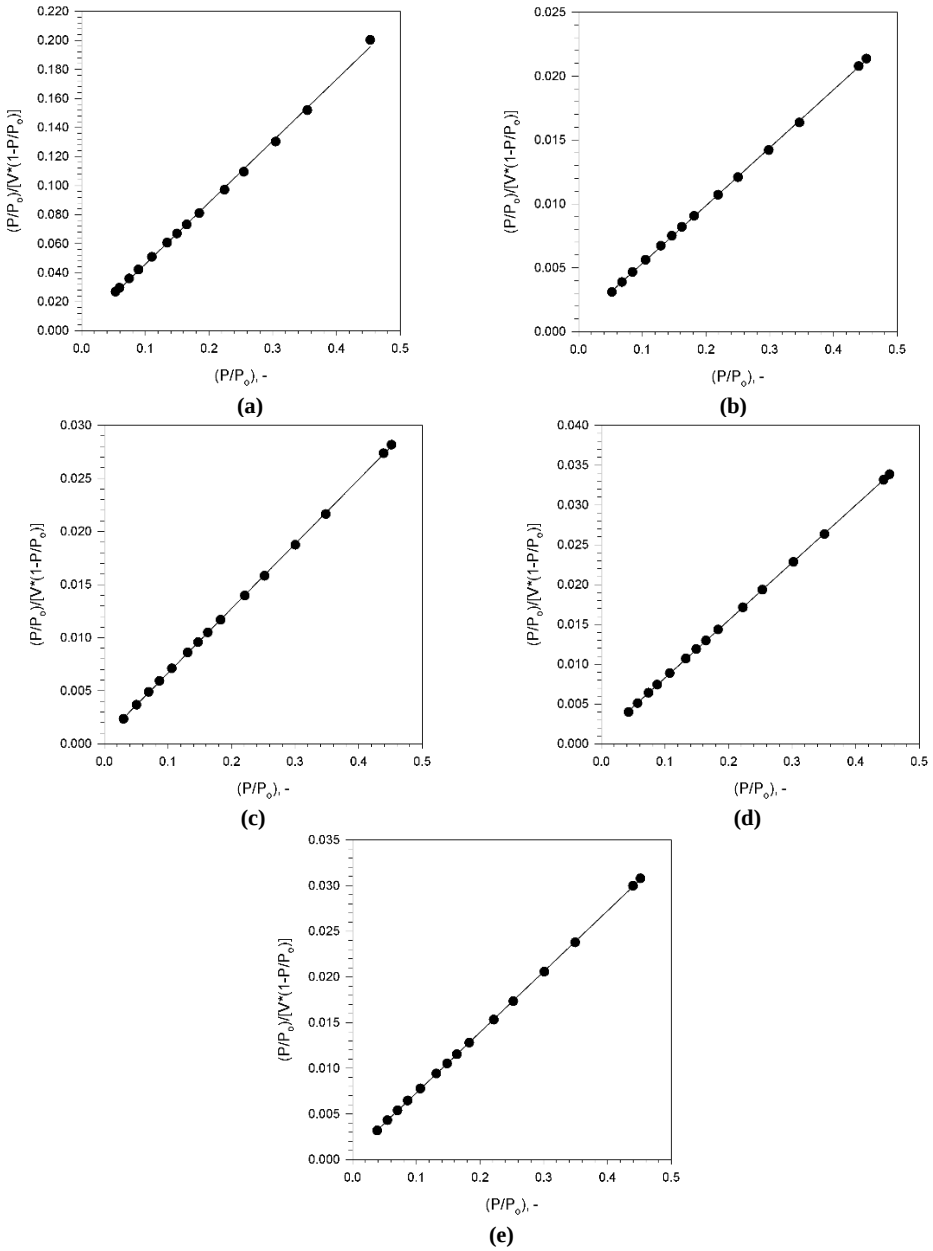

Fig. 4. N_2 adsorption isotherm by the BET model for (a) 13X zeolite (b) FeX zeolite (c) TiO_2/FeX zeolite (d) ZnO/FeX zeolite (e) TiO_2+ZnO/FeX zeolite

Table 1. The parameters and R^2 for the isotherm models

Isotherm model		13X zeolite	FeX zeolite	TiO_2/FeX zeolite	ZnO/FeX zeolite	TiO_2+ZnO/FeX zeolite
Langmuir	V_m, cm^3/g	74.07	227.27	208.33	312.50	204.08
	K_L, l/mmHg	0.0003	0.0010	0.0008	0.0004	0.0008
	R^2, -	0.0217	0.241	0.1645	0.0572	0.1495
Freundlich	K_f, $cm^3/g/(mmHg)^{1/n}$	0.0397	1.1638	1.0748	0.5467	0.8658
	n, -	1.0595	1.5017	1.5436	1.3424	1.4896
	R^2, -	0.7185	0.8408	0.7939	0.7968	0.8012
BET	V_m, cm^3/g	9.62	21.79	16.39	13.62	14.99
	C, -	76.85	51.00	87.14	73.40	95.29
	R^2, -	0.9999	0.9997	0.9999	0.9999	0.9999

The 13X zeolite displayed a low capacity of 9.62 cm^3/g, which significantly increased to 21.79 cm^3/g following the ion exchange of FeX zeolite, likely due to the activation of surface sites. However, after loading TiO_2 onto the TiO_2/FeX zeolite, the capacity declined sharply to 16.39 cm^3/g, and remained low at 13.62 cm^3/g after ZnO was loaded solo onto the ZnO/FeX zeolite. A slight uptick was observed after the combined loading of TiO_2 and ZnO onto the TiO_2+ZnO/FeX zeolite, rising to 14.99 cm^3/g. These results indicate that, while the mesoporous structure remained relatively stable, as confirmed by the BET model, the chemical alterations made at each treatment stage directly impacted the adsorption efficiency. In contrast to a prior study [57] higher adsorption capacities were reported for NaX and FeX, due to smaller particle sizes compared to the present study. Larger particle sizes tend to have a lower surface area-to-volume ratio, which can potentially reduce the availability of active sites and result in diminished adsorption performance.

The main feature evaluated by the BET model was the surface area, which was calculated and listed in Table 2. The calculated values were 104.37 m^2/g for 13X zeolite, 94.79 m^2/g for FeX zeolite, 71.33 m^2/g for TiO_2/FeX zeolite, 59.28 m^2/g for ZnO/FeX zeolite, and 65.20 m^2/g for TiO_2+ZnO/FeX zeolite. The surface area of 13X zeolite is lower than that measured for NaX zeolite [11] and 13X zeolite [58]. This discrepancy may result from variations in the raw zeolite source, as factors like purity, initial moisture content, impurity levels, storage conditions, and the grinding and sieving process can all influence the zeolite's surface properties. Additionally, the change in particle size distribution after grinding may alter the accessibility of micropores, further influencing the measured surface area. For the current FeX sample, the surface area was also less than that of FeX zeolite [11] and Fe_2O_3-13X [58]. The reduction in surface area for the FeX zeolite in this study, compared to earlier findings, may be attributed to variations in ion exchange conditions, including iron solution concentration, exchange duration, and temperature. These factors may cause some iron ions to deposit partially within the micropores or on the internal surfaces of the zeolite, blocking specific pore channels and consequently reducing the effective surface area. Furthermore, uneven distribution of iron ions within the porous structure might also explain the decrease in observed surface area values.

The BET surface area of TiO_2/FeX zeolite surpassed that of TiO_2/natural zeolite [59] and TiO_2/natural zeolite [60]; however, the BET surface area was greater than that of TiO_2/ZSM-5 [61]. The higher BET surface area of TiO_2/FeX zeolite compared to TiO_2/natural zeolite can be explained by the more ordered pore structure and enhanced initial purity of the synthetic 13X zeolite, which facilitates better dispersion of TiO_2 nanoparticles.

In comparison to TiO_2/ZSM-5, the TiO_2/FeX composite exhibited a greater surface area, likely due to the more open pore structure of 13X zeolite. On the other hand, ZSM-5 has a denser and narrower channel system, which restricts surface accessibility. The BET surface area of ZnO/FeX was lower than that of ZnO/NaY zeolite and ZnO/Na-a zeolite [62, 63]. The reduced BET surface area of ZnO/FeX relative to ZnO/NaY and ZnO/Na-a zeolite can be attributed to variations in framework structure and pore volume, as Y-type zeolites typically have larger supercages and greater mesoporosity, enabling better ZnO dispersion and resulting in a higher surface area, while Na-a zeolite has a tighter and more limited pore system.

Additionally, the t-plot method is crucial for accurately evaluating the surface area and pore volumes of mesoporous zeolites. In the t-plot, the N_2 adsorption volume was plotted versus the thickness of the adsorbed layer (in nm) as shown in Fig. 5. As shown in Fig. 5 (a) and Fig. 5 (b), FeX zeolite has a significantly larger N_2 adsorption capacity across all t values compared to the 13X zeolite. This result indicates that the ion exchange process (Na with Fe(II)) has positively contributed to the increase in adsorption capacity. Furthermore, Fig. 5 (c), Fig. 5(d), and Fig. 5 (e) unequivocally show a decrease in N_2 adsorption after the loading of semiconductors. In contrast, the step of adding semiconductors to the FeX zeolite was accompanied by an apparent decrease in the ability to absorb N_2, as shown in Fig. 5 (c), Fig. 5 (d), and Fig. 5 (e), and these results were in good agreement with previous works [64, 65].

The external surface area described by the t-plot is calculated using the Halsey Eq. 5. The internal surface area (S_{int}) was calculated by subtracting the external surface area (S_{ext}) from the total surface area obtained by the BET model (S_{BET}), and the results are listed in Table 2.

4.3. BJH pore diameter and volume

The N_2 adsorption-desorption measurements of 13X zeolite, FeX zeolite, TiO_2/FeX zeolite, ZnO/FeX zeolite, and TiO_2+ZnO/FeX zeolite were used to determine the pore size distribution via Eq. 6, and they were plotted in Fig. 6.

The pore size distribution for FeX zeolite (Fig. 6, b) was noted to be narrower than that of the other materials (Fig. 6 a, c, d, and e), indicating a more consistent pore size. The calculated mode pore size diameter was tabulated in Table 3, and was 6.91 nm for 13X zeolite, 1.87 nm for FeX zeolite, and 2.12 nm for each of TiO_2/FeX zeolite, ZnO/FeX zeolite, and TiO_2+ZnO/FeX zeolite. Variations in total pore volumes were also evident among the adsorbents, with values of 0.3166 cm^3/g for 13X zeolite, 0.2528 cm^3/g for FeX zeolite, 0.2339 cm^3/g for TiO_2/FeX zeolite, 0.2314 cm^3/g for ZnO/FeX zeolite, and 0.2228 cm^3/g for TiO_2+ZnO/FeX zeolite. FeX zeolite exhibited not only a narrower pore size distribution but also the highest total pore volume. Moreover, the addition of TiO_2 or ZnO to the FeX zeolite led to slightly decreased total pore volumes compared to FeX zeolite.

Table 2. Specific surface area of different modified zeolites

zeolite	Specific surface area, m^2/g			Reference
	S_{BET}	S_{ext}	S_{int}	
13X	104.37	16.12	88.25	Current study
Na-X	569.14	-	-	[11]
13X	573.00	-	-	[58]
Fe-X	94.79	8.34	86.45	Current study
FeX	213.31	-	-	[11]
Fe_2O_3-13X	541.00	-	-	[58]
TiO_2/ FeX	71.33	7.53	63.80	Current study
TiO_2/ natural zeolite	31.4	-	-	[60]
TiO_2/ZSM5 (TZ2600)	47.10	-	-	[61]
ZnO/FeX	59.28	6.55	52.72	Current study
ZnO /NaY	417.8	35.7	382.1	[62]
ZnO/Na A	91.73	-	-	[63]
TiO_2+ZnO/FeX	65.20	6.87	58.33	Current study

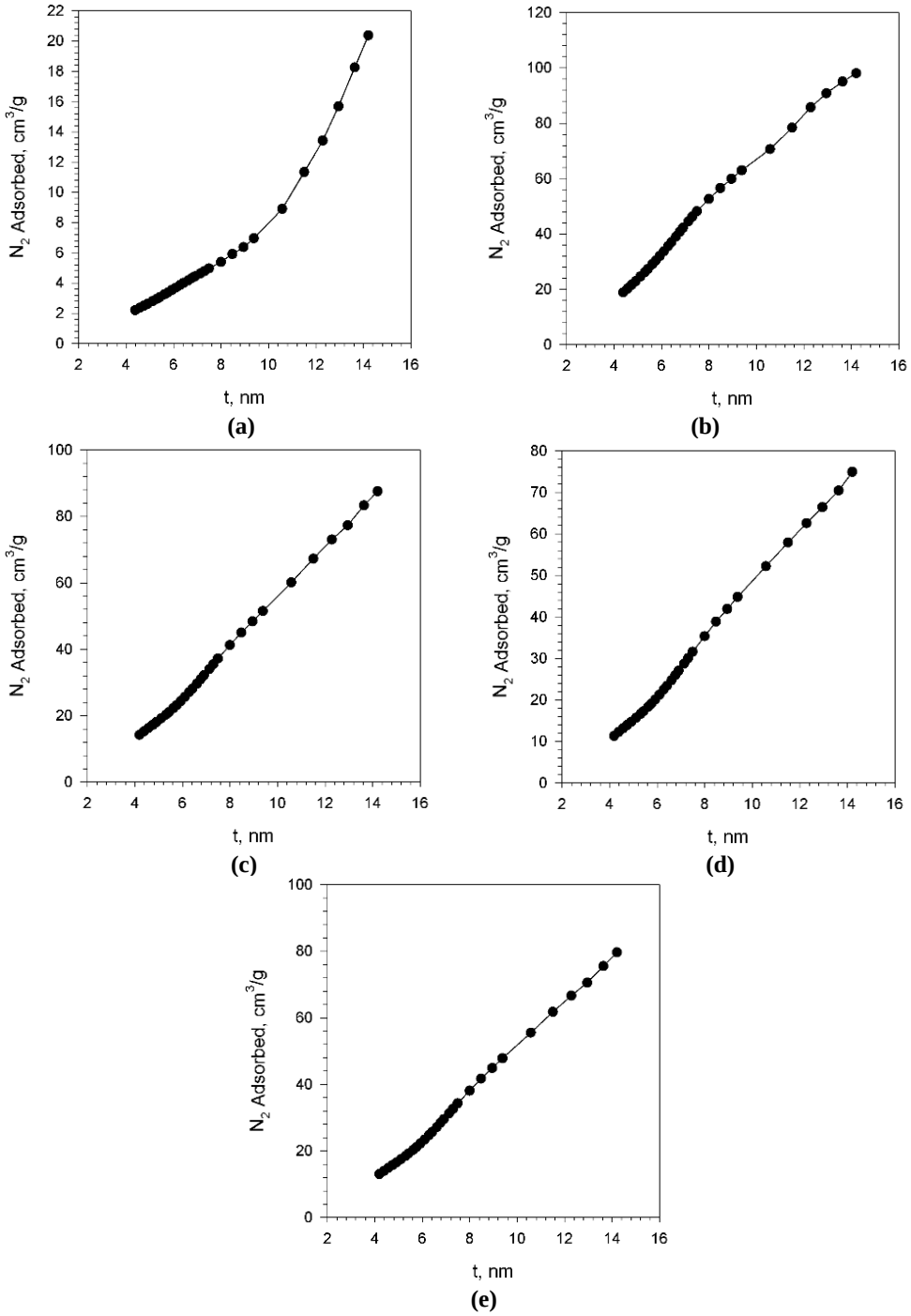

Fig. 5. The t-plot for (a) 13X zeolite (b) FeX zeolite (c) TiO_2/FeX zeolite (d) ZnO/FeX zeolite (e) TiO_2+ZnO/FeX zeolite

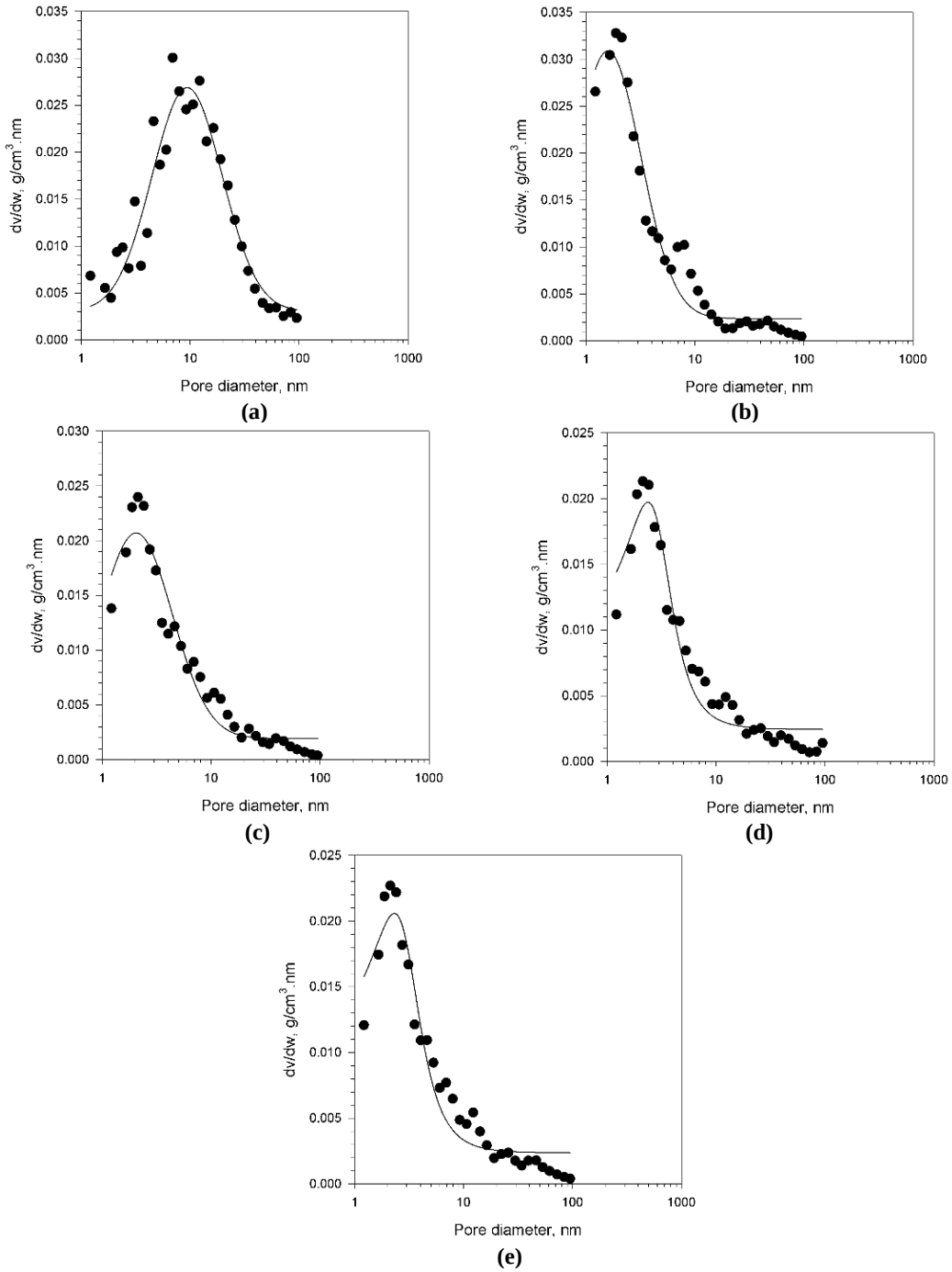

Fig. 6. BJH pore size distribution for (a) 13X zeolite (b) FeX zeolite (c) TiO_2/FeX zeolite (d) ZnO/FeX zeolite (e) TiO_2+ZnO/FeX zeolite

Table 3. The BJH pore diameter and volume of different modified zeolites

Zeolite	d_{BJH}, nm	V_p, cm^3/g	Reference
13X	6.91	0.3166	Current study
Na-X	2.45	0.3490	[11]
13X	2.30	0.3600	[58]
FeX	1.87	0.2528	Current study
FeX	5.19	0.2768	[11]
Fe_2O_3-13X	2.60	0.2100	[58]
TiO_2/FeX	2.12	0.2339	Current study
TiO_2/ natural zeolite	-	0.067	[60]
TiO_2/ZSM5 (TZ2600)	-	-	[61]
ZnO/FeX	2.12	0.2228	Current study
ZnO /NaY	-	-	[62]
ZnO/Na A	22.60	0.0005	[63]
TiO_2+ZnO/FeX	2.12	0.2228	Current study

5- Conclusion

The physical adsorption-desorption technique of nitrogen gas was employed to investigate the textural properties of zeolite samples and modified zeolites by ion exchange and incorporation of semiconductor oxides on their surface. The studied zeolites showed IUPAC type IV adsorption isotherms with distinct hysteresis types H2, H3, and H4, indicating a mesoporous structure. The obtained experimental data for the studied zeolites did not conform to the Langmuir and Freundlich adsorption models, indicating that the adsorption process was neither ideal nor straightforward. This implies that multiple potential mechanisms were involved in the adsorption. The Langmuir model assumes uniform adsorption on the surface and a monolayer. In contrast, the Freundlich model is empirical and ignores saturation effects, rendering both models insufficient for accurately describing actual adsorption behavior. Conversely, the BET model provided the best fit to the experimental data for all tested samples and was used to estimate the total surface area values of the zeolites. The calculated surface area of the zeolites decreased with the modification and addition steps, and the external surface area also exhibited a similar behavior according to the Halsey model. A significant decrease in surface area was observed upon the addition of TiO_2 and ZnO, which was attributed to the partial blockage or filling of the zeolite pores by these semiconductor metal oxide particles. These findings were supported by the results of the BJH model, which demonstrated that FeX zeolite exhibited the narrowest pore size distribution and the highest pore volume. Meanwhile, the addition of TiO_2 and ZnO resulted in a slight decrease in the overall pore volume without significantly changing the pore size. The treated samples exhibited distinct surface characteristics, indicating that the modification processes significantly altered the physical properties of the zeolite.

References

[1] P. Rożek, M. Król, and W. Mozgawa, "Geopolymer-zeolite composites: A review," *Journal of Cleaner Production*, vol. 230, pp. 557–579, May 2019, https://doi.org/10.1016/j.jclepro.2019.05.152

[2] B. M. Kurji, I. M. Mujtaba, and A. S. Abbas, "Synthesis, Characterizations, and Recent Applications of the Silica-based Mobil Composition of Mesoporous Material: A Review," *Iraqi Journal of Chemical and Petroleum Engineering*, vol. 24, no. 3, pp. 1–12, Sep. 2023, https://doi.org/10.31699/IJCPE.2023.3.1

[3] W. J. Roth, P. Nachtigall, R. E. Morris, and J. Čejka, "Two-dimensional zeolites: Current status and perspectives," *Chemical Reviews*, vol. 114, no. 9, pp. 4807–4837, Feb. 2014, https://doi.org/10.1021/cr400600f

[4] T. Derbe, S. Temesgen, and M. Bitew, "A Short Review on Synthesis, Characterization, and Applications of Zeolites," *Advances in Materials Science and Engineering*, vol. 2021, no. 1, pp. 1–17, Sep. 2021, https://doi.org/10.1155/2021/6637898

[5] A. Primo and H. Garcia, "Zeolites as catalysts in oil refining," *Chemical Society Reviews*, vol. 43, no. 22, pp. 7548–7561, Mar. 2014, https://doi.org/10.1039/C3CS60394F

[6] N. Jiang, R. Shang, S. G. J. Heijman, and L. C. Rietveld, "High-silica zeolites for adsorption of organic micro-pollutants in water treatment: A review," *Water Research*, vol. 144, pp. 145–161, Jul. 2018, https://doi.org/10.1016/j.watres.2018.07.017

[7] J. M. Castillo, J. Silvestre Albero, F. Rodriguez-Reinoso, T. J. H. Vlugt, and S. Calero, "WATER ADSORPTION IN HYDROPHILIC ZEOLITES: EXPERIMENT AND SIMULATION," *Physical Chemistry Chemical Physics*, vol. 15, no. 40, pp. 17374–17382, Aug. 2013, https://doi.org/10.1039/C3CP52910J

[8] W. Song, Y. Wei, and Z. Liu, "Chemistry of the Methanol to Olefin Conversion," in *Zeolites in Sustainable Chemistry: Synthesis, Characterization and Catalytic Applications*, F.-S. Xiao and X. Meng, Eds., Springer Berlin Heidelberg, 2016, pp. 299–346. https://doi.org/10.1007/978-3-662-47395-5_9

[9] I. W. Nah, K. Y. Hwang, and Y. G. Shul, "A simple synthesis of magnetically modified zeolite," *Powder Technology*, vol. 177, no. 2, pp. 99–101, Feb. 2007, https://doi.org/10.1016/j.powtec.2007.02.044

[10] D. W. Astuti, Mudasir, and N. H. Aprilita, "Preparation and characterization adsorbent based on zeolite from Klaten, Central Java, Indonesia," *Journal of Physics: Conference Series*, vol. 1156, no. 1, pp. 5–11, 2019, https://doi.org/10.1088/1742-6596/1156/1/012002

[11] S. K. Kamal and A. S. Abbas, "Textural Properties Characterization for NaX and FeX Zeolites by Nitrogen Adsorption-desorption Technique," *Iraqi Journal of Chemical and Petroleum Engineering*, vol. 23, no. 4, pp. 33–41, Dec. 2022, https://doi.org/10.31699/IJCPE.2022.4.5

[12] H. Mousavi, J. Towfighi Darian, and B. Mokhtarani, "Enhanced nitrogen adsorption capacity on Ca^{2+} ion-exchanged hierarchical X zeolite," *Separation and Purification Technology*, vol. 264, no. 1, p. 118442, Feb. 2021, https://doi.org/10.1016/j.seppur.2021.118442

[13] R. K. Abid and A. S. Abbas, "Adsorption of organic pollutants from real refinery wastewater on prepared cross-linked starch by epichlorohydrin," *Data Brief*, vol. 19, pp. 1318–1326, Aug. 2018, https://doi.org/10.1016/J.DIB.2018.05.060

[14] Z. A. Hammood, T. F. CHYAD, and R. AL-SAEDI, "ADSORPTION PERFORMANCE OF DYES OVER ZEOLITE FOR TEXTILE WASTEWATER TREATMENT," *Ecological Chemistry and Engineering S*, vol. 28, no. 3, pp. 329–337, Sep. 2021, https://doi.org/10.2478/eces-2021-0022

[15] S. K. A. Barno, H. J. Mohamed, S. M. Saeed, M. J. Al-Ani, and A. S. Abbas, "Prepared 13X Zeolite as a Promising Adsorbent for the Removal of Brilliant Blue Dye from Wastewater," *Iraqi Journal of Chemical and Petroleum Engineering*, vol. 22, no. 2, pp. 1–6, Jun. 2021, https://doi.org/10.31699/IJCPE.2021.2.1

[16] T. P. Belova, "Adsorption of heavy metal ions (Cu^{2+}, Ni^{2+}, Co^{2+} and Fe^{2+}) from aqueous solutions by natural zeolite," *Heliyon*, vol. 5, no. 9, p. e02320, Sep. 2019, https://doi.org/10.1016/J.HELIYON.2019.E02320

[17] S. M. Al-Jubouri *et al.*, "Multicomponent Equilibrium Isotherms and Kinetics Study of Heavy Metals Removal from Aqueous Solutions Using Electrocoagulation Combined with Mordenite Zeolite and Ultrasonication," *Applied Science and Engineering Progress*, vol. 18, no. 1, pp. 7484–7484, Jan. 2025, https://doi.org/10.14416/J.ASEP.2024.07.011

[18] S. K. Kamal, Z. M. Mustafa, and A. S. Abbas, "Reaction Kinetics and Mass Transfer of Photocatalytic Fenton for Phenol Degradation in a Petroleum Refinery Wastewater," *Tikrit Journal of Engineering Sciences*, vol. 32, no. 1, p. 1743, Mar. 2025, https://doi.org/10.25130/tjes.32.1.30

[19] E. Erdem, N. Karapinar, and R. Donat, "The removal of heavy metal cations by natural zeolites," *Journal of Colloid and Interface Science*, vol. 280, no. 1, pp. 309–314, Sep. 2004, https://doi.org/10.1016/j.jcis.2004.08.028

[20] H. L. Tran, M. S. Kuo, W. D. Yang, and Y. C. Huang, "Study on Modification of NaX Zeolites: The Cobalt (II)-Exchange Kinetics and Surface Property Changes under Thermal Treatment," *Journal of Chemistry*, vol. 2016, pp. 1–7, Mar. 2016, https://doi.org/10.1155/2016/1789680

[21] E. V. Kuznetsova, E. N. Savinov, L. A. Vostrikova, and V. N. Parmon, "Heterogeneous catalysis in the Fenton-type system FeZSM-5/H_2O_2," *Applied Catalysis B: Environmental*, vol. 51, no. 3, pp. 165–170, Mar. 2004, https://doi.org/10.1016/j.apcatb.2004.03.002

[22] E. Nyankson *et al.*, "Synthesis and characterisation of zeolite-A and Zn-exchanged zeolite-A based on natural aluminosilicates and their potential applications," *Cogent Engineering*, vol. 5, no. 1, Feb. 2018, https://doi.org/10.1080/23311916.2018.1440480

[23] W. Chunfeng, J. Li, S. Xia, W. Lianjun, and S. Xiuyun, "Evaluation of zeolites synthesized from fly ash as potential adsorbents for wastewater containing heavy metals," *Journal of Environmental Sciences*, vol. 21, no. 1, pp. 127–136, May 2009, https://doi.org/10.1016/S1001-0742(09)60022-X

[24] L. Bacakova, M. Vandrovcova, I. Kopova, and I. Jirka, "Applications of zeolites in biotechnology and medicine-a review," *Biomaterials Science*, vol. 6, no. 5, pp. 974–989, Mar. 2018, https://doi.org/10.1039/C8BM00028J

[25] A. El Gaidoumi, A. Chaouni Benabdallah, B. El Bali, and A. Kherbeche, "Synthesis and Characterization of Zeolite HS Using Natural Pyrophyllite as New Clay Source," *Arabian Journal for Science and Engineering*, vol. 43, no. 1, pp. 191–197, Jul. 2018, https://doi.org/10.1007/s13369-017-2768-8

[26] Y. T. Tran, J. Lee, P. Kumar, K. H. Kim, and S. S. Lee, "Natural zeolite and its application in concrete composite production," *Composites Part B: Engineering*, vol. 165, pp. 354–364, May 2019, https://doi.org/10.1016/j.compositesb.2018.12.084

[27] M. Król, "Natural vs. Synthetic zeolites," *Crystals (Basel)*, vol. 10, no. 7, p. 622, Jul. 2020, https://doi.org/10.3390/cryst10070622

[28] T. Pan, Z. Wu, and A. C. K. Yip, "Advances in the green synthesis of microporous and hierarchical zeolites: A short review," *Catalysts*, vol. 9, no. 3, p. 274, Mar. 2019, https://doi.org/10.3390/catal9030274

[29] A. Khaleque *et al.*, "Zeolite synthesis from low-cost materials and environmental applications: A review," *Environmental Advances*, vol. 2, pp. 1–24, Oct. 2020, https://doi.org/10.1016/j.envadv.2020.100019

[30] D. Kerstens, B. Smeyers, J. Van Waeyenberg, Q. Zhang, J. Yu, and B. F. Sels, "State of the art and perspectives of hierarchical zeolites: practical overview of synthesis methods and use in catalysis," *Advanced Materials*, vol. 32, no. 44, pp. 1–52, 2020, https://doi.org/10.1002/adma.202004690

[31] Z. Asgar Pour and K. O. Sebakhy, "A Review on the Effects of Organic Structure-Directing Agents on the Hydrothermal Synthesis and Physicochemical Properties of Zeolites," *Chemistry*, vol. 4, no. 2, pp. 431–446, May 2022, https://doi.org/10.3390/chemistry4020032

[32] J. A. Rabo and M. W. Schoonover, "Early discoveries in zeolite chemistry and catalysis at Union Carbide, and follow-up in industrial catalysis," *Applied Catalysis A: General*, vol. 222, no. 1–2, pp. 261–275, Dec. 2001, https://doi.org/10.1016/S0926-860X(01)00840-7

[33] P. Y. Dapsens, C. Mondelli, and J. Pérez-Ramírez, "Design of Lewis-acid centres in zeolitic matrices for the conversion of renewables," *Chemical Society Reviews*, vol. 44, no. 20, pp. 7025–7043, Apr. 2015, https://doi.org/10.1039/C5CS00028A

[34] W. Reschetilowski, "Catalysis on Zeolites and Zeolite-like Materials II," *Catalysts*, vol. 14, no. 7, p. 460, Jul. 2024, https://doi.org/10.3390/catal14070460

[35] B. A. Alshahidy and A. S. Abbas, "Preparation and modification of 13X zeolite as a heterogeneous catalyst for esterification of oleic acid," in *AIP Conference Proceedings*, American Institute of Physics Inc., Mar. 2020, p. 020167. https://doi.org/10.1063/5.0000257

[36] N. Diban *et al.*, "TiO_2–Zeolite Metal Composites for Photocatalytic Degradation of Organic Pollutants in Water," *Catalysts*, vol. 11, no. 11, p. 1367, Nov. 2021, https://doi.org/10.3390/catal11111367

[37] F. H. Kamil, S. K. A. Barno, F. Shems, A. Jihad, and A. S. Abbas, "Photocatalytic Degradation of Sulfamethoxazole from a Synthetic Pharmaceutical Wastewater Using Titanium Dioxide (TiO_2) Powder as a Suspended Heterogeneous Catalyst," *Iraqi Journal of Industrial Research (IJOIR)*, vol. 10, no. 1, pp. 26–33, Apr. 2023, https://doi.org/10.53523/ijoirVol10I1ID314

[38] M. Nawaz, A. A. Khan, A. Hussain, J. Jang, H. Y. Jung, and D. S. Lee, "Reduced graphene oxide−TiO_2/sodium alginate 3-dimensional structure aerogel for enhanced photocatalytic degradation of ibuprofen and sulfamethoxazole," *Chemosphere*, vol. 261, Jul. 2020, https://doi.org/10.1016/j.chemosphere.2020.127702

[39] S. Mergenbayeva, T. S. Atabaev, J. Vakros, D. Mantzavinos, and S. G. Poulopoulos, "Photocatalytic Degradation of 4-tert-butylphenol Using Solar Light Responsive Ag_2CO_3," *Catalysts*, vol. 12, no. 12, pp. 1–15, Nov. 2022, https://doi.org/10.3390/catal12121523

[40] S. Mergenbayeva *et al.*, "Degradation of 4-Tert-Butylphenol in Water Using Mono-Doped (M1: Mo, W) and Co-Doped (M2-M1: Cu, Co, Zn) Titania Catalysts," *Nanomaterials*, vol. 12, no. 14, pp. 1–20, Jul. 2022, https://doi.org/10.3390/nano12142326

[41] H. Park, Y. Park, W. Kim, and W. Choi, "Surface modification of TiO_2 photocatalyst for environmental applications," *Journal of Photochemistry and Photobiology C: Photochemistry Reviews*, vol. 15, pp. 1–20, Oct. 2013, https://doi.org/10.1016/j.jphotochemrev.2012.10.001

[42] T. Ayorinde and C. M. Sayes, "An updated review of industrially relevant titanium dioxide and its environmental health effects," *Journal of Hazardous Materials Letters*, vol. 4, pp. 1–7, Aug. 2023, https://doi.org/10.1016/j.hazl.2023.100085

[43] [43] A. Moezzi, A. M. McDonagh, and M. B. Cortie, "Zinc oxide particles: Synthesis, properties and applications," *Chemical Engineering Journal*, vol. 185–186, pp. 1–22, Jan. 2012, https://doi.org/10.1016/j.cej.2012.01.076

[44] A. Kolodziejczak-Radzimska and T. Jesionowski, "Zinc oxide-from synthesis to application: A review," *Materials*, vol. 7, no. 4, pp. 2833–2881, Apr. 2014, https://doi.org/10.3390/ma7042833

[45] C. G. Silva *et al.*, "Developing highly active photocatalysts: Gold-loaded ZnO for solar phenol oxidation," *Journal of Catalysis*, vol. 316, pp. 182–190, May 2014, https://doi.org/10.1016/j.jcat.2014.05.010

[46] V. N. Jafarova and G. S. Orudzhev, "Structural and electronic properties of ZnO: A first-principles density-functional theory study within LDA(GGA) and LDA(GGA)+U methods," *Solid State Communications*, vol. 325, pp. 1–5, 2021, https://doi.org/10.1016/j.ssc.2020.114166

[47] X. Chen, "Modeling of Experimental Adsorption Isotherm Data," *Information*, vol. 6, no. 1, pp. 14–22, Jan. 2015, https://doi.org/10.3390/info6010014

[48] N. Ayawei, A. N. Ebelegi, and D. Wankasi, "Modelling and Interpretation of Adsorption Isotherms," *Journal of Chemistry*, vol. 2017, pp. 1–11, Sep. 2017, https://doi.org/10.1155/2017/3039817

[49] B. M. Kurji and A. S. Abbas, "Comparative Study of Textural Properties for Various Silica by Nitrogen Adsorption-desorption Technique," *Egyptian Journal of Chemistry*, vol. 65, no. 132, pp. 313–320, Dec. 2022, https://doi.org/10.21608/EJCHEM.2022.125169.5568

[50] V. G. Baldovino-Medrano, V. Niño-Celis, and R. Isaacs Giraldo, "Systematic Analysis of the Nitrogen Adsorption-Desorption Isotherms Recorded for a Series of Materials Based on Microporous-Mesoporous Amorphous Aluminosilicates Using Classical Methods," *Journal of Chemical and Engineering Data*, vol. 68, no. 9, pp. 2512–2528, Sep. 2023, https://doi.org/10.1021/acs.jced.3c00257

[51] V. S. Achari, A. S. Rajalakshmi, S. Jayasree, and R. M. Lopez, "Surface Area and Porosity Development on Granular Activated Carbon by Zirconium: Adsorption Isotherm studies," *Journal of Applied Research and Technology*, vol. 16, no. 3, pp. 211–228, Jun. 2018, https://doi.org/10.22201/icat.16656423.2018.16.3.719

[52] A. Marcilla, A. Gomez-Siurana, M. Ma José, and F. J. Valdés, "Comments on the Methods of Characterization of Textural Properties of Solids from Gas Adsorption Data," *Adsorption Science & Technology*, vol. 27, no. 1, pp. 69–84, Apr. 2009, https://doi.org/10.1260/026361709788921579

[53] MAGEE R. W., "Evaluation of the External Surface Area of Carbon Black by Nitrogen Adsorption," *Rubber Chemistry & Technology*, vol. 68, no. 4, pp. 590 – 600, Sep. 1995, https://doi.org/10.5254/1.3538760

[54] O. F. Baugh, E. P. Barrett, L. G. Joyner, and P. P. Halenda, "The Determination of Pore Volume and Area Distributions in Porous Substances. I. Computations from Nitrogen Isotherms," *Journal of the American Chemical Society*, vol. 73, no. 1, pp. 373–380, Jan. 1951, https://doi.org/10.1021/ja01145a126

[55] J. Choma, M. Jaroniec, and M. Kloske, "Improved Pore-size Analysis of Carbonaceous Adsorbents," *Adsorption Science & Technology*, no. 3, pp. 307–315, 2002, https://doi.org/10.1260/026361702760254487

[56] D. Dollimore and G. R. Heal, "Pore-Size Distribution in Typical Adsorbent Systems," *Journal of Colloid and Interface Science*, vol. 33, no. 4, pp. 508–519, Mar. 1970, https://doi.org/10.1016/0021-9797(70)90002-0

[57] S. K. Kamal and A. S. Abbas, "Decrease in the organic content of refinery wastewater by photocatalytic Fenton oxidation using iron-doped zeolite: Catalyst preparation, characterization, and performance," *Chemical Engineering and Processing - Process Intensification*, vol. 193, pp. 1–9, Nov. 2023, https://doi.org/10.1016/j.cep.2023.109549

[58] A. A. AbdulRazak and S. Rohani, "Sodium Dodecyl Sulfate-Modified Fe2O3/Molecular Sieves for Removal of Rhodamine B Dyes," *Advances in Materials Science and Engineering*, vol. 2018, pp. 1–10, May 2018, https://doi.org/10.1155/2018/3849867

[59] K. V. S. and T. A. Dontsova, "Potential Applications Of TiO_2/Natural Zeolite Composites For Dye Removal," *Water and Water Purification Technologies. Scientific and Technical News*, vol. 38, no. 1, pp. 27–36, Aug. 2024, https://doi.org/10.20535/2218-930012024314044

[60] G. Zhang, A. Song, Y. Duan, and S. Zheng, "Enhanced photocatalytic activity of TiO2/zeolite composite for abatement of pollutants," *Microporous and Mesoporous Materials*, vol. 255, pp. 61–68, 2018, https://doi.org/10.1016/j.micromeso.2017.07.028

[61] S. Mergenbayeva *et al.*, "TiO_2/Zeolite Composites for SMX Degradation under UV Irradiation," *Catalysts*, vol. 14, no. 2, p. 147, Feb. 2024, https://doi.org/10.3390/catal14020147

[62] V. R. Batistela, L. Z. Fogaça, S. L. Fávaro, W. Caetano, N. R. C. Fernandes-Machado, and N. Hioka, "ZnO supported on zeolites: Photocatalyst design, microporosity and properties," *Colloids and Surfaces A: Physicochemical and Engineering Aspects*, vol. 513, pp. 20–27, 2017, https://doi.org/10.1016/j.colsurfa.2016.11.023

[63] L. K. Munguti and F. B. Dejene, "High Photodegradation Performance of ZnO Nanoparticles Supported on Porous Zeolite Na-a: Effects of ZnO Loading," *Materials Chemistry and Physics*, 295, 2023, https://doi.org/10.1016/j.matchemphys.2022.127063

[64] J. Pires, R. Fernandes, M. L. Pinto, and M. Batista, "Microporous Volumes from Nitrogen Adsorption at 77 K: When to Use a Different Standard Isotherm?," *Catalysts*, vol. 11, no. 12, p. 1544, Dec. 2021, https://doi.org/10.3390/catal11121544

[65] A. Galarneau, F. Villemot, J. Rodriguez, F. Fajula, and B. Coasne, "Validity of the t-plot method to assess microporosity in hierarchical micro/mesoporous materials," *Langmuir*, vol. 30, no. 44, pp. 13266–13274, Sep. 2014, https://doi.org/10.1021/la5026679

تأثير إضافة Fe(II) عن طريق التبادل الأيوني وترسيب أشباه الموصلات المختلفة على الخصائص النسيجية لزيوليت 13X

روان حيدر علي [١]، سامي محمد زبون [١]، عمار صالح عباس [١،*]

١ قسم الهندسة الكيمياوية، كلية الهندسة، جامعة بغداد، بغداد، العراق

الخلاصة

تناولت هذه الدراسة دراسة الخواص النسيجية لزيوليت 13X، و زيوليت FeX، و زيوليت TiO_2/FeX، و زيوليت ZnO/FeX، و زيوليت TiO_2+ZnO/FeX، باستخدام بيانات امتزاز–امتصاص النيتروجين عند درجات حرارة منخفضة ثابتة. أشار منحنى الامتزاز–الامتزاز إلى أن المواد المدروسة لها بنية مسامية متوسطة من النوع الرابع، وفقًا لتعريف الاتحاد الدولي للكيمياء البحتة و التطبيقية. أشارت نتائج تحليل بيانات امتزاز النيتروجين باستخدام نماذج لانجموير، و فروينديليش، و بروناور–إيميت–تيلر إلى أن نموذج بروناور–إيميت–تيلر هو الأنسب لوصف البيانات. استُخدم نموذج باريت، و جوينر، و هالیندا لتحليل توزيع حجم المسام، وقطر المسام، و متوسط حجم المسام للمواد الماصة. بعد عملية التبادل الأيوني والتحميل، لوحظ انخفاض ملحوظ في مساحة السطح و قيم توزيع حجم المسام، بينما كان الانخفاض في حجم المسام ضئيلاً. أظهر الزيوليت 13X قطر مسام أكبر، مما يشير إلى حدوث بعض التلف الهيكلي أو تكوين مسام أوسع ضمن نطاق المسام المتوسطة أثناء خطوات التبادل الأيوني أو التعديل بإضافة أكاسيد أشباه الموصلات. في المقابل، أظهر الزيوليت FeX حجم مسام أصغر، مما يدل على بنية مسامية دقيقة أكثر إحكاما. في حين أظهرت الزيوليتات المعدلة – TiO_2 و ZnO و TiO_2+ZnO – بنية مسام متناسقة، مما يشير إلى مسامية متوسطة مستقرة مع حجم مسام أصغر، فإن هذا يعني أن بعض مسام الزيوليت كانت مسدودة أو مملوءة بجزيئات TiO_2 وZnO.

الكلمات الدالة: الامتصاص، معادلة درجة حرارة الامتزاز الفيزيائي، البنية المسامية المتوسطة، توزيع حجم المسام، مساحة السطح.